

To appear in AJ.

# Quantitative Morphology of the Intermediate-Redshift Galaxy Cluster Abell 2443 from Ground-Based Imaging – Evidence for a galaxy concentration index correlation with cluster density

I. Trujillo

*Instituto de Astrofísica de Canarias, E-38200, La Laguna, Tenerife, Spain*

itc@ll.iac.es

J.A.L. Aguerri

*Astronomische Institut der Universität Basel, Venusstrasse 7, CH-4102 Binningen, Switzerland*

and

C.M. Gutiérrez and J. Cepa

*Instituto de Astrofísica de Canarias, E-38200, La Laguna, Tenerife, Spain*

## ABSTRACT

We present broad-band photometry and provide a quantitative analysis of the structure of galaxies in the inner region of the Abell Cluster 2443 ( $z \sim 0.1$ ). The galaxy parameters have been derived by fitting a two-component model (Sérsic  $r^{1/n}$  bulge and exponential disk) to a magnitude-limited sample. Using a new method of analysis which takes into account the effects of seeing on the structural parameters and considers the ellipticity as an active parameter, we avoid systematic errors arising from assumptions of circular symmetry. 76% of the sample galaxies were classified with these models, the rest were morphologically peculiar. For the spiral galaxies, the relation between  $n$  and  $B/D$  is consistent with the trend observed in nearby field galaxy samples. The Sérsic index  $n$  (which can be considered as a concentration index) of the elliptical galaxies is correlated with the local surface density of the cluster. Monte Carlo simulations were used to check the reliability of the method and determine the magnitude selection criteria.

*Subject headings:* galaxies: distances and redshift—galaxies: evolution—galaxies: photometry—galaxies: fundamental parameters

## 1. Introduction

Following the discovery of the Butcher & Oemler (1978, 1984) effect considerable observational effort has been devoted to understanding the change in the properties of the galaxies in high density environments. Only recently, thanks to the high spatial resolution imaging achieved with the *Hubble Space Telescope* (*HST*) and the improvement in the ground-based observations, it has been established that the morphological properties of galaxies in rich clusters at intermediate redshift differ dramatically from those in nearby clusters. There is an increase in the number of spiral population, a factor of 2–3 less S0 galaxies, and the fraction of ellipticals is already as large as, or larger than, in nearby clusters. Most of the observational work has been developed in the range  $z=0.3-0.5$  (Couch et al. 1994, 1998; Dressler et al. 1994; Wirth, Koo, & Kron 1994; Dressler et al. 1997; Oemler, Dressler, & Butcher 1997; Smail et al. 1997). Few studies have been done in the  $z \sim 0.1-0.2$  regime (Fasano et al. 2000) which is a crucial range for a better understanding of galaxy evolution in dense environments.

The claimed morphological evolution of galaxies in distant clusters is based, mostly, on visual classifications of these objects. This classification system is based on the Hubble scheme, in which the ratio of the spheroidal to the disk components is a key parameter differentiating between elliptical and spiral galaxies. Visual classifications were developed on the basis of nearby, bright normal galaxies (Sandage 1961; Sandage & Tammann 1987), and are founded on the assumption that the structure of galaxies follows certain archetypes. But, the ability to classify visually by Hubble type is increasingly difficult for faint and/or high-redshift galaxies, and it is therefore necessary to use a quantitative profile decomposition method to retrieve the physical properties of the observed galaxies. Quantitative classification has two major advantages over visual classification: (1) it is reproducible, and (2) biases can be understood and carefully characterized through simulations that are treated as real data. The Hubble deep field (HDF) is a good example where, for the same sample of galaxies, different classification schemes have been applied (visual: van den Bergh et al. 1996, non-parametric: Abraham et al. 1996 and profile decomposition: Marleau & Simard (1998)) obtaining substantially different results.

The use of quantitative morphology enables the recovery of reliable information on the structural parameters (shape, size, axial ratios, etc.) of the galaxies. The information contained in the structural parameters play an important role that is required to understand the evolution and origin of galaxies. Visual morphology classification must be considered only as the first step in the detailed studies of the properties of the galaxies in high density environments. Furthermore, galaxies in dense regions are undergoing tidal friction, high-speed impulse encounters and mergers. These processes can affect the density profile of the galaxies and must be compared with those from field galaxies.

Automatic classification systems are based on the fitting of structural models to the surface-brightness profiles of galaxies. In this case it is assumed that the surface-brightness profile of every structural component follows some analytical law. Nowadays, the spheroidal component is usually

modeled with a Sérsic profile (Sérsic 1968) and the disk component with an exponential law. An alternative scheme is based on non-parametric model-independent classification in which galaxies are classified using some quantitative index such as color, concentration, and asymmetry of the galactic light distribution (e.g., Bershady, Jangren, & Conselice 2000).

Seeing scatters light from objects, producing a loss of resolution in the images. Morphological classification based on visual inspection from ground-based images is therefore compromised as redshift increases. For the same reason, classification systems based on concentration and asymmetry are also degraded with redshift and need be corrected for the effects of seeing. Methods based on fitting structural components to the surface-brightness profile of the galaxies can be corrected (Schade et al. 1996).

In a previous paper (Trujillo et al. 2001a), we studied the effects of the seeing on Sérsic profiles. We quantified how ignoring these effects on the observed surface brightness distribution results in significantly different structural parameters, and consequently different dynamical properties inferred from these parameters. In order to recover the seeing-free structural parameters of distant objects, we presented the mathematical basis for an accurate description of the seeing effects on surface brightness distributions following  $r^{1/n}$  laws.

In this paper, we develop a fitting routine to estimate the structural properties of galaxies from the inner region of the intermediate-redshift ( $z=0.103$ ) rich cluster Abell Cluster 2443 following the mathematical analysis developed in our previous paper. The characteristics of this cluster (richness and distance) provide an ideal data set for the study of the structural parameters in an insufficiently probed regime of  $z$ . Section 2 describes the photometric decomposition algorithm. In §3 we present the results of simulations that test the reliability of the method for measuring galactic structural parameters from ground-based images of a simulated galaxy sample. Section 4 describes the results of the photometric decomposition technique applied to the galaxies in the inner region of Abell Cluster 2443.

## 2. The Fitting Algorithm

The typical scale size of galaxies studied at intermediate redshift is comparable to the seeing obtained with ground-based telescopes (barring adaptive/active optics). It is therefore absolutely necessary to consider the effects of seeing on the images, and very accurate convolutions of the point spread function (PSF) and the model profiles of the galaxies are required. Most current fitting algorithms have two main disadvantages: a) the surface brightness is assumed to be circularly symmetric, and b) the convolution procedure is executed using fast Fourier transforms. In case a) the ellipticity parameter is measured usually for the outer most isophotes as a parameter external to the fit. This procedure ignores the fact that the seeing distorted surface-brightness distribution is a function of the seeing and the intrinsic ellipticity of the object. In case b), even if the elliptical symmetry of the objects is taken into account, the fast Fourier transform is not appropriate when

there are strong changes in the spatial scale of the galaxy profile. Most of the profiles in common use (e.g. de Vaucouleurs, Sérsic) have such shapes. The inner parts of the galaxy profiles are steep, and this demands a very accurate measure of the high frequencies in the Fourier domain. Consequently, flatter distributions are obtained as a result of a convolution using the fast Fourier transform compared with the traditional methods integrating in the real domain.

The uncertainty in the estimation of the structural parameters also depends on the signal-to-noise ratio. Decreasing signal-to-noise implies a greater degeneracy in the possible parameters that fit the same profile. So, it is important to establish a limiting magnitude where the recovery of parameters is reliable. This acquires special significance in the bulge + disk decomposition. Insufficiently deep images might mask the disk component of some galaxies. When a bulge and disk decomposition is tried on these objects a systematically *lower* fractional bulge-to-total luminosity ( $B/T$ ) ratio is obtained. This is because the disk component of the fit, due to the absence of points in the outer parts of the galaxy, increases its slope to fit the transition region between the bulge and disk; overestimated disks are expected (see the next section). This problem can also be present in nearby samples (e.g., Prieto et al. 1992).

To minimize the above mentioned problems, we have developed a tool that takes into account the effects of seeing on elliptical structures. The mathematical basis of the algorithm is described by Trujillo et al. (2001a). Briefly, the fitting procedure works using elliptical coordinates  $(\xi, \theta)$  defined as:

$$\begin{aligned} x &= \xi \cos \theta \\ y &= \xi(1 - \epsilon) \sin \theta \end{aligned} \tag{1}$$

where a different ellipticity,  $\epsilon$ , is used for each component.

Ellipses are fitted to the objects using the ELLIPSE task from the IRAF package. The surface-brightness profile along the semi-major axis (the  $\xi$  axis) and the isophotal ellipticity profile are fitted simultaneously. The ellipticity profile is uniquely determined for any given seeing and set of structural parameters. The intrinsic ellipticity is assumed to be constant for all the isophotes.

The goal in correcting the observed profiles for the effects of seeing is to recover the true intrinsic galaxy light profile. Normally, one does this by assuming an initial model that represents the intrinsic galaxy profile and then convolving this with the PSF, iterating until convergence. However, if the galaxy has elliptical symmetry not only are the inner isophotes circularized, but the outer isophotes may also be distorted by seeing. More importantly, although the convolution of a model which is assumed to be spherically symmetric will fit the observed data, recovered parameters will not represent the true intrinsic galaxy profile. This is because the convolution of an elliptical 2D model is different to the convolution of a spherical 2D model. We have therefore performed the convolution of elliptical two-dimensional models following Trujillo et al (2001a). Not doing this can result in systematic errors.

Two different kinds of PSFs are available in our fitting procedure: Gaussian and Moffat-type

(Moffat 1969). These PSFs are convolved with our surface brightness profile models. A Levenberg–Marquardt non-linear fitting algorithm (Press et al. 1992) was used to determine the parameter set which minimizes  $\chi^2$ . Extensive Monte-Carlo simulations were done to check the method and estimate the uncertainties in the recovered parameters. In particular, the simulations allow us (see Section 3) to gain an understanding of the limiting magnitude where the procedure is able to obtain reliable results.

### 2.1. The two-dimensional Surface-Brightness Profile Model

If the intermediate-redshift galaxy population has a roughly similar distribution of morphological properties as the nearby population, then structures such as bars, dust lanes, spiral structures, galaxy cores, etc., can be neglected due to the small angle scale subtended by these structures at these distances. On the other hand, it is expected that any significant evolution in the galaxy morphology at these redshift ranges will leave its imprint in the form of anomalous values of the parameters, or an excess of peculiar galaxies that can not be parameterized.

The 2D fitted galaxy model has two components (an  $r^{1/n}$  bulge and an exponential disk) with a total of seven parameters: the bulge effective intensity,  $I_e$ , the bulge effective radius,  $r_e$ , the Sérsic index,  $n$ , the bulge ellipticity,  $e_b$  ( $e \equiv 1 - b/a$ ,  $b \equiv$  semi-minor axis,  $a \equiv$  semi-major axis), the disk central intensity,  $I_0$ , the exponential disk scale length,  $h$ , and the disk ellipticity,  $e_d$ . The 2D bulge component is a Sérsic (1968) profile of the form:

$$I(\xi) = I_e 10^{-b[(\xi/r_e)^{(1/n)} - 1]}. \quad (2)$$

The parameter  $b$  is set equal to  $0.868n - 0.142$ , so that  $r_e$  remains the projected radius enclosing half of the light in this component (Capaccioli 1989). The de Vaucouleurs profile is obtained when  $n = 4$ . The second, “disk”, component is a simple exponential profile of the form:

$$I(\xi) = I_0 e^{(\xi/h)}. \quad (3)$$

The presence of a “disk” component does not imply the presence of a rotational disk since many virially supported systems also have simple exponential profiles.

## 3. Monte-Carlo Simulations

We have performed Monte-Carlo simulations to test the reliability of our method. First, we tested the ability to recover parameters from bulge-only (i.e. purely elliptical) structures, and then we explored the possibility of carrying out accurate bulge + disk decompositions. In both cases we created 150 artificial galaxies with structural parameters randomly distributed in the following ranges:

- a) for bulge-only structures:  $16 \leq I \leq 20$ ,  $0''.44 \leq r_e \leq 1''.65$ ,  $0.5 \leq n \leq 6$ , and  $0 \leq \epsilon \leq 0.6$  (the lower limit on  $n$  is due to the physical restrictions pointed out in Trujillo et al. 2001a);
- b) for bulge + disk structures:  $16 \leq I \leq 20$ ,  $0''.2 \leq r_e \leq 0''.88$ ,  $0.5 \leq n \leq 4$ ,  $0 \leq \epsilon_b \leq 0.4$ ,  $0''.55 \leq h \leq 1''.65$ ,  $0 \leq B/T \leq 0.65$ , and  $0 \leq \epsilon_d \leq 0.6$ .

No correlation between the input structural parameters was imposed. We also studied the possibility that our algorithm introduces an artificial correlation between the recovered parameters by applying a 2D Kolmogorov-Smirnov test (Fasano & Franceschini 1987) between the input random data distribution ( $n$ ,  $r_e$ ) and the output one. The significance level of this analysis was 0.27<sup>1</sup> indicating that the output distribution was also random. So, no artificial correlations between the output parameters was found.

The artificial galaxies were created by using the IRAF task MKOBJECT. To simulate the real conditions of our observations of the Abell Cluster A2443 (see next section), we added a background sky image (free of sources) taken from our  $I$ -band image (see description below); the dispersion in the sky determination was 0.1%. The seeing in the simulation was set at  $0.88''$  (FWHM), as in our observations. The PSF was assumed to be Gaussian and known exactly. The pixel scale for all simulations was  $0''.11 \text{ pixel}^{-1}$  to match our prime-focus imaging. We follow the same procedure to process both the simulated and actual data.

### 3.1. Bulge-Only Structures

Figure 1 shows the relative error between the input and output parameters. This figure also shows the mean relative errors as a function of the magnitude. We have divided our simulations into bins of 0.5 mag and computed for each bin the mean relative error between the input and output magnitudes,  $r_e$ , and  $n$ . We have also obtained the mean differences between the input and output ellipticity. The total number of simulations (150) resulted in an average number of about 20 objects per bin. All the parameters can be obtained with an relative error less than 10% for objects brighter than  $I$  magnitude 19.25 (see Table 1). No systematic errors were found for objects brighter than this magnitude, which can be considered a strict limiting magnitude for the determination of the structural parameters.

The limiting magnitude is of course a function of the signal-to-noise ratio but not in the normal manner. Better signal-to-noise permits us to obtain reliable parameters from fainter galaxies. From simulations we found that an increase by a factor 2 in the signal-to-noise allowed us to determine the structural parameters for objects two magnitudes fainter. This is because the local slope of the surface brightness profiles is a decreasing function of the radius, so the outermost regions of the profiles are flatter than the inner ones. Having fixed a detection threshold (i.e.  $I=19$ ), which

---

<sup>1</sup>When the significance level is  $> 0.20$  the two data sets are not significantly different

depends on the signal-to-noise factor, there is a rapid increase in the number of points available to fit the profiles in the outermost regions as the signal-to-noise factor increases.

The difference between the recovered Sérsic index, which defines the type of profile, and the input value is shown in Figure 2 as a function of  $n$ . There is no obvious bias in the  $n$  parameter recovered from the simulations. Most studies of this kind systematically give lower values of output  $n$  for larger input  $n$  (e.g., Marleu & Simard 1998). The reason for this is the assumption of circular symmetry in the profile models. This can bias the analysis, and hence conclusions of studies performed at different redshifts. For instance, higher redshift galaxies will appear smaller, and are consequently more affected by the PSF. Not correcting the ellipticity results in the derivation of smaller values of  $n$  for these systems, and therefore effects claims of structural evolution. We have avoided this problem by taking into account the ellipticity of the objects in our fitting routine.

### 3.2. Bulge + Disk Structures

The recovery of the real bulge and disk structural parameters is strongly dependent on the signal-to-noise and the  $B/T$  ratio of the objects. In cases of low signal-to-noise the disk component can be masked by the noise. This can produce an over-estimation of the disk, as explained before, which simultaneously affects the estimation of the bulge parameters (e.g., Schade et al. 1996). Sufficiently bright disks do not have this problem, but intermediate and large  $B/T$  galaxies suffer when there is insufficient signal-to-noise (or equivalent low total magnitudes of the objects). This bias may complicate the nature of the trend between decreasing  $B/T$  and redshift reported by Marleau & Simard (1998). From this consideration, it is clearly necessary to establish a limiting magnitude where the estimation of the parameters are reliable.

Figure 3 shows the relative error between the input and output parameters, and the mean relative errors, as a function of the magnitude. As in §3.1, the simulations were divided into 0.5 magnitude bins. For each bin, the mean relative error between input and output bulge and disk magnitudes,  $r_e$ ,  $n$ , and  $h$  was computed. The mean differences between the input and output ellipticities for the bulge and disk structures were also evaluated. Apart from the effective radius, all the parameters can be obtained to an accuracy of better than 10% for galaxies with an I-band magnitude brighter than 18.75 (see Table 2).

Figure 4 shows  $d(B/T) \equiv B/T(\text{measured}) - B/T(\text{input})$  and mean  $d(B/T)$  versus  $B/T(\text{input})$  and scale length. We divided the simulations into 0.1 bins ( $B/T$ ), the mean differences in  $d(B/T)$  going from  $B/T = 0$  to  $B/T = 0.65$  were: 0.08 ( $\sigma = 0.15$ ), 0.02 (0.09), 0.03 (0.09), 0.03 (0.08), 0.02 (0.19),  $-0.02$  (0.16), and 0.05 (0.19). We distinguish between points brighter and fainter than 18.75 magnitudes. Our results establish that the  $B/T$  relation (which is one of the most important parameters for classifying the galaxies) and the scale-length  $h$  can be recovered well to the limiting magnitude. As expected, smaller disks (i.e. a bigger  $B/T$  ratio) have the greater dispersions in the  $B/T$  recoveries. This result is dependent on the total magnitude of the object (or equivalently, the

signal-to-noise). It is important to stress that the results discussed here for bulges, or bulge + disk structures, are conservative (errors less than 10%).

#### 4. The Abell Cluster 2443 ( $z = 0.103$ )

Abell 2443 is a rich southern cluster (richness class 2 and Bautz–Morgan type II) at  $z = 0.103$ . Its brightest cluster member, PGC 068859 (identified in our study as ID = 1), was first cited in the VLA survey of rich clusters (Slee, Perley, & Siegman 1989).

##### 4.1. Observations and Data Reduction

Observations were obtained on August 19, 1998, at the 2.5 m Nordic Optical Telescope (NOT) at the Observatorio del Roque de los Muchachos on La Palma. The prime focus CCD camera was used with pixel scale of  $0''.11 \text{ pixel}^{-1}$  and the seeing ranged from FWHM  $0''.88$  to  $1''$ . The field was observed through  $B$ ,  $V$ , and  $I$  filters with equal integration times ( $3 \times 900 \text{ s}$ ) and in the  $R$  filter ( $3 \times 600 \text{ s}$ ). The mean seeing was  $0''.88$  (FWHM) in the  $I$  images (which were used to investigate the morphology). The observed field ( $2'.5 \times 2'.5$ ) covered the central part of the cluster, which was the inner 300 kpc assuming throughout that  $H_0 = 75 \text{ km s}^{-1} \text{ Mpc}^{-1}$ .

We applied the standard data reduction procedures: bias subtraction, flat fielding correction, flux calibration using Landolt (1992) standards, addition of images of the same filter, and sky subtraction. Figure 5 shows the reduced and calibrated image of the cluster in the  $I$  band. The large extended object at the center is the cD galaxy PGC 068859.

We used the SExtractor galaxy photometry package (Bertin & Arnouts 1996, version 2.1.4) on the images. This package is optimized to detect and measure sources from astronomical images. Basically, SExtractor detects all sources from an image above a LOWTHRESHOLD, and which have an area greater than a MINAREA. These two parameters are given as input to the program. For our extractions we have taken LOWTHRESHOLD =  $1.5 \sigma$  and MINAREA = 4 pixels, where  $\sigma$  is the standard deviation of the sky background of the images. To get rid of stars we have only studied extended sources.

A cross-correlation search between the  $R$  and  $I$  images enabled us to identify 250 extended objects to  $I = 23 \text{ mag}$ . From these, we selected 121 objects that were identified in all four bands. Broad-band aperture photometry of these objects was done using SExtractor in all the above mentioned filters (see Table 3). The magnitudes were computed using a variable aperture for each object. The radius of this aperture was  $2.5 r_{\text{Kron}}$ , where  $r_{\text{Kron}}$  is the Kron radius (see Kron 1980). This radius is obtained from the luminosity profile of each individual object and is different for each object. From our simulations, the threshold magnitude for an accurate morphological structure analysis is  $I = 19 \text{ mag}$ . This criteria left us with 33 objects.



## 4.2. Results and Discussion

Two different kinds of model fitting were performed: a) a two-dimensional bulge + disk decomposition, and b) a two-dimensional fitting of a Sérsic law (i.e. one structural component). Both models were fitted for all 33 galaxies selected. A similar study was carried out using the *R*-band filter but no significant deviations were found. We found eight (24%) galaxies that could not be fitted by our routine (ID: 2, 5, 8, 35, 40, 49, 77, and 90). We hereafter refer to these objects as “peculiar” galaxies since many of them exhibit peculiar visual morphologies. This left a total of 25 galaxies. Figure 6 shows the I-band images of each, along with the radial profile and ellipticity, and the residuals from the fits.

Galaxies which satisfy  $B/T > 0.6$  (19/33) are referred as “ellipticals” and their parameters are presented in Table 5. For these galaxies a better fit to the profile was found using only a Sérsic component model. We use the term “elliptical” to refer to galaxies that are better fitted with one (Sérsic law) component, without necessarily implying a virially supported system. Those galaxies with  $B/T < 0.6$  (6/33) are listed in Table 4. The cD galaxy (ID: 1) was classified by our algorithm as a galaxy with  $B/T < 0.6$ . cD galaxies are not “standard” ellipticals, in fact, these galaxies present envelopes which may be detected as a separate component in  $r^{1/4}$  plots (Graham et al. 1995). Our algorithm tries to fit the presence of this ‘extra’ light in the outer parts of the galaxy by adding an extra component to the profile. By fitting only the inner 5 arcsec with a pure Sérsic profile, the best fit is achieved for  $n=1.96$ . This technique was also used by Graham et al (1995) and similar values of  $n$  are given in their sample. Because of the “special” characteristics of these kind of galaxies we have decided not to include them in the group of “ellipticals”.

As in most similar studies, contamination from foreground and background objects is a source of uncertainty. In Figure 7 we plot  $(B - I)$  versus  $I$  magnitudes. This figure shows two clearly differentiated branches, a red one,  $(B - I) > 3$ , and another in which the bulk of the galaxies have  $(B - I) < 3$ . We have been able to model five galaxies in the redder branch. These five galaxies (ID: 26, 29, 85, 86, and 129) have all been labeled as “ellipticals” and have high values of  $n$  ( $n > 4.8$ ). Also, three of these galaxies (29, 85, and 86) are near our  $I=19$  cut off limit. It is certainly possible that these galaxies are field (background) galaxies with a disk component (e.g., Saglia et al. 1997) that we are not able to resolve. Therefore, to err on the side of caution, we assumed that  $(B - I) > 3$  galaxies may be background galaxies and are not taken into consideration hereafter. Galaxies belonging to the cluster,  $(B - I) < 3$ , exhibit reasonable values of their parameters with the exception of object 6. Visual inspection suggests that this object might be an edge on spiral galaxy that our algorithm mis-classifies. We also exclude this object hereafter. Object 11 might be a disk galaxy too but it presents a reasonable fit and values of the recovered parameters, so in order to be consistent with our procedure we have maintained it as an elliptical object.

Quantitative morphology permits us to investigate correlations between the different structural parameters with those obtained for nearby galaxy samples. In Figure 8 we plot  $n$  versus the logarithm of the bulge-to-disk luminosity ratio,  $\log(B/D)$ , for the galaxies with  $B/T < 0.6$ . There

is a clear correlation between these two quantities, as exists for local field galaxies (Andredakis, Peletier, & Balcells 1995; Graham 2001). There are not enough galaxies to investigate any significant departure (i.e. evolution) from the results of these authors. The Freeman (1970) relation is also shown in Figure 8. Our results are in good agreement with this relation (solid line). To evaluate the absolute magnitude of these galaxies we assumed that the galaxies belong to the cluster and the  $K$ -correction was implemented following Poggianti (1997).

Figure 9 shows the relation between the Sérsic indexes  $n$  and a) the (projected) distance from the brightest central cluster member (PGC 068859) and b) the local cluster surface density (Dressler 1980). We present separately the values of  $n$  for the bulge + disk galaxies and the  $n$  values from the “elliptical” galaxies. The values of  $n$  for the “spiral galaxy” bulges are, on average, smaller than those obtained for the “ellipticals”. To measure the local cluster surface density, the ten nearest (projected) neighbors to each of the analyzed galaxies were found, after computing the area involved and correcting for the field galaxy density<sup>2</sup> the local surface density (galaxies  $\text{Mpc}^{-2}$ ) was evaluated down to  $I = 23$ . The data reveal that elliptical galaxies with higher values of  $n$  are located in the inner part of the cluster. The Pearson’s  $r_p$  correlation coefficient between  $n$  and central distance is  $r_p=-0.45$ ; if we exclude object 11, we obtain  $r_p=-0.64$ . Similarly, elliptical galaxies with larger  $n$  reside in regions of higher cluster surface density. Here, the correlation is stronger,  $r_p=0.63$ , and  $r_p=0.76$  excluding object 11. We can obtain similar results using the, perhaps more meaningful, central galaxy concentration as defined by Trujillo, Graham, & Caon (2001):

$$C_{r_e}(\alpha) = \frac{\sum_{i,j \in E(\alpha r_e)} I_{ij}}{\sum_{i,j \in E(r_e)} I_{ij}}. \quad (4)$$

Here,  $E(r_e)$  is the isophote which encloses half of the total light of the galaxy, and  $E(\alpha r_e)$  is the isophote at a radius  $\alpha(< 1)$  times  $r_e$ . Specifically, for a Sérsic law one obtains that  $C_{r_e}(\alpha)$  increases monotonically with  $n$

$$C_{r_e}(\alpha) = \frac{\gamma(2n, k\alpha^{1/n})}{\gamma(2n, k)}, \quad (5)$$

with  $k = 2n - 0.324$  and where  $\gamma(a, x)$  is the incomplete gamma function (Abramowitz & Stegun 1964). Figure 10 shows the relation between the central galaxy concentration of each galaxy and a) the (projected) distance from the brightest central cluster member and b) the local cluster surface density with  $\alpha = 0.3$ . The values for the Pearson’s coefficient are similar than obtained using  $n$ :  $r_p=-0.45$  and  $-0.56$  (excluding object 11) for the correlation between  $C_{r_e}$  and distance, and  $r_p=0.68$  ( $r_p=0.74$  removing object 11) for the correlation between  $C_{r_e}$  and the local cluster surface density.

---

<sup>2</sup>To correct for field galaxy contamination, galaxies with  $(B - I) > 3$  were not taken into account when computing the density.

The dispersion presents in these relations might be inflated by the fact that both the central distance and the local surface density are “projected” parameters. If the relation that we have found for A2443 is shown to hold for other clusters, it means that the qualitative morphology-density relation noted by previous authors (e.g. Dressler 1980; Dressler et al. 1997; Fasano et al. 2000) extends further and can be placed on a quantitative basis, such that the detailed structure of the individual galaxies (beyond the broad elliptical/spiral distinction) is related to their immediate environment/density. The brightest cluster galaxies, which reside at the dense centers of galaxy clusters, are known to contain multiple nuclei (Postman & Lauer 1995) from mergers. They also possess high values of  $n$ , or are better described by power laws (Graham et al. 1996). What we may well be observing here is an extension of this behavior to less massive systems and lower cluster densities.

Strom & Strom (1978) noted that the structural properties of Elliptical galaxies are related to the dynamical properties of their parent clusters. By tidal friction and high-speed impulse encounters they were able to explain why characteristic sizes of the galaxies decrease by a factor of 1.5 or more in the denser regions of the clusters. But tidal stripping seems not be the answer to explain the previously shown correlations. In fact, galaxy central concentration is an observed core property due to it is defined in the inner part (within the effective radius) of the object. “Encounters which lead to the stripping of halo stars should not affect the distribution of stars in the tightly bound cores of the galaxies” (Strom & Strom 1978). Also, in simulations, “models whose initial surface densities are described by an  $r^{1/4}$  (de Vaucouleurs) law are still well fitted by such a law after collisions in which the target galaxy loses up to 40 percent of its mass” (Aguilar & White 1986). Moreover, “the  $r^{1/n}$  models are stable to radial and non radial perturbations” (Ciotti 1991). These statements seem to indicate that the global structure (index  $n$  or central concentration) of the galaxies must be only conditioned by mechanisms which act over the complete structure (not only in the outer parts).

Against an explanation based on tidal stripping exists another evidence: Graham, Trujillo & Caon (2001) have simulated the loss of stars in the outer parts of the galaxies by truncating  $r^{1/n}$  profiles and remeasuring the actual effective radius and, consequently,  $C_{re}$ . By doing this they find that truncated galaxies tend to be less concentrated than galaxies which extend to infinity.

Favoring that what we are seeing is an effect of mechanisms which act over the global structure are: a) mergers tend to increase the concentration of the galaxies. As an example, numerical simulations (White 1983; Barnes 1990; Barnes 1992) have supported the hypothesis that mergers between typical disk galaxies ( $n=1$ ) produce remnants with the overall morphology and structural parameters of elliptical galaxies ( $n=4$ ), b) the concentration (or index  $n$ ) correlates with global structure parameters of the galaxies such as total luminosity, or equivalently mass. (Caon et al. 1993; Young & Currie 1994; Jerjen & Binggeli 1997).

Reasons exposed before suggest that the increase in the central galaxy concentration (that is, the larger values of  $n$ ) as a function of the cluster surface density may be a consequence of

mergers, but also, an alternative to this, may be that the galaxies with larger  $n$ , that is, larger central concentration, may have formed from primordial fluctuations of greater amplitude during a subclustering process. Theories of gravitational collapse and galaxy formation must be able to distinguish between these two alternatives.

## 5. Summary

We have presented broad-band  $B$ ,  $V$ ,  $R$ , and  $I$  photometry of 121 galaxies brighter than  $I=23$  in the inner region of Abell Cluster 2443. We have modeled the surface-brightness profiles from 33 of these objects and have obtained reliable quantitative morphological classifications for 25 objects down to  $I = 19$  mag, the remaining 8 being morphologically peculiar. Our structural analysis procedure has been tested through Monte Carlo simulations. We have overcome two systematic problems that usually effect such fitting algorithms in the past. Firstly, we do not evaluate the ellipticity as an external parameter measured from the ellipticity of the outer isophotes; instead, we have taken into account that the seeing-affected surface-brightness profile is a function of the intrinsic ellipticity of the objects. Secondly, we have avoided the numerical problems associated with the use of fast Fourier transforms to compute the convolution between the surface brightness profile models and the PSF of the images when dealing with very steep intensity profiles. We have determined the seeing-corrected central galaxy concentration (related to the Sérsic index). We reveal correlations between this parameter and the projected distance to the brightest cluster member and also with the projected cluster surface density. This is possibly due to a larger number of mergers in the high-density zones of the cluster. It is hoped through the study of more clusters that one will be able to determine the strength and possible universality of this relationship, and learn important clues to the nature of galaxy formation.

JALA was supported by grant 20-56888.99 from the Schweizerischer Nationalfonds. Nordic Optical Telescope is operated on the island of La Palma jointly by Denmark, Finland, Iceland, Norway, and Sweden, in the Spanish Observatorio del Roque de los Muchachos of the Instituto de Astrofísica de Canarias.

We are indebted to Alister W. Graham who kindly proof-read versions of this manuscript. The authors are grateful to the anonymous referee for the valuable refereeing that helped us to improve the rigor and clarity of this paper.

## REFERENCES

- Abraham, R. G., Tanvir, N. R., Santiago, B. X., Ellis, R. S., Glazebrook, K. G., & van den Bergh, S. 1996, MNRAS, 279, L47.
- Abramowitz M., Stegun I., 1964, Handbook of Mathematical Functions. Dover, New York

- Aguilar, L.A. & White, S.D.M, 1986, *ApJ*, 307, 97
- Andredakis, Y. C., R. F. Peletier, & Balcells, M. 1995, *MNRAS*, 275, 874
- Barnes, J. 1990, in *Dynamics and Interactions of Galaxies*, ed. R. Wielen (Heidelberg: Springer-Verlag), 232
- Barnes, J. 1992, *ApJ*, 393, 484
- Bershady, M. A., Jangren, A., & Conselice, C. 2000, *AJ*, 119, 2645
- Bertin, E. & Arnout, S. 1996, *A&AS*, 117, 393
- Butcher, H., & Oemler, A., Jr. 1978, *ApJ*, 226, 559
- Butcher, H., & Oemler, A., Jr. 1984, *ApJ*, 285, 426
- Caon, N., Capaccioli, M., & D’Onofrio, M. 1993, *MNRAS*, 265, 1013
- Capaccioli, M. 1989, in *The World of Galaxies*, ed. H. G. Corwin & L. Bottinelli (Berline: Springer-Verlag), p.208.
- Ciotti, L. 1991, *A&A*, 249, 99
- Couch, W.J., Ellis, R. S., Sharples, R. M., & Smail, I., 1994, *ApJ*, 430, 121
- Couch, W.J., Barger, A. J., & Smail, I., Ellis, R. S., Sharples, R. M., 1998, *ApJ*, 497, 188
- Dressler, A. 1980, *ApJ*, 236, 351
- Dressler, A., Oemler, A. Jr., Butcher, H., Gunn, J. E., 1994, *ApJ*, 430, 107
- Dressler, A., Oemler, A. Jr., Couch, W. J., Smail, I., Ellis, R. S., Barger, A., Butcher, H., Poggianti, B. M., Sharples, R. M. 1997 *ApJ*, 490, 577
- Fasano, G., & Franceschini, A., 1987, *MNRAS*, 225, 155
- Fasano, G., Poggianti, B. M., Couch, W.J., Bettoni, D., KJaergaard, P., & Moles, M. 2000, *ApJ*, 542, 673
- Freeman, K. 1970, *ApJ*, 160, 811
- Graham, A. W., Lauer T., Colles M., Postman M., 1996, *ApJ*, 465, 534
- Graham, A. W. 2001, *AJ*, in press
- Graham, A. W., Trujillo, I., & Caon, N., 2001, *AJ*, submitted
- Jerjen, H. & Binggeli, B. 1997, in *The Nature of Elliptical Galaxies; The Second Stromlo Symposium*, ASP Conf. Ser., 116, 239

- Kron, R. G. 1980, *ApJS*, 43, 305
- Landolt, A. 1992, *AJ*, 104, 340
- Marleau, F. R., & Simard, L. 1998, *ApJ*, 507, 585
- Moffat, A. F. J. 1969, *A&A*, 3, 455
- Oemler, A., Jr., Dressler, A., & Butcher, H., 1997, *ApJ*, 474, 561
- Poggianti, B. M. 1997, *A&AS*, 122, 399
- Postman, M. & Lauer T., 1995, *ApJ*, 440, 28
- Press, W. H., Teukolsky, S. A., Vetterling, W. T., & Flannery, B. P. 1992, *Numerical Recipes* (Cambridge; Cambridge Univ. Press)
- Prieto, M., Beckman, J. E., Cepa, J., & Varela, A. M. 1992, *A&A*, 257, 85.
- Saglia, R. P., Bertschinger, E., Baggle, G., Burstein, D., Colless, M., Davies, R. L., McMahan, R. K., Jr., & Wegner, G. 1997, *ApJS*, 109, 79
- Sandage, A. R. 1961, *The Hubble Atlas of Galaxies* (Washington: Carnegie Inst. Washington)
- Sandage, A. R., & Tammann, G. A. 1987, *A Revised Shapley–Ames Catalog of Bright Galaxies* (Washington: Carnegie Inst. Washington)
- Schade, D., Lilly, S. J., Le Fèvre, O., Hammer, F., & Crampton, D. 1996, *ApJ*, 464, 79.
- Slee, O. B., Perley, R. A., & Siegman, B. C. 1989, *Australian J. Phys.*, 42, 633
- Sérsic, J. 1968, *Atlas de Galaxias Australes Córdoba: Obs. Astronómico*
- Smail, I., Dressler, A., Couch, W.J., Ellis, R. S., Oemler, A., Jr., Butcher, H., & Sharples, R. M. 1997, *ApJS*, 110, 213
- Strom, S. E. & Strom, K.M. 1978, *ApJ*, 225, L93
- Trujillo, I., Aguerri, J. A. L., Cepa, J., & Gutiérrez, C. M. 2001a, *MNRAS*, 321, 269
- Trujillo, I., Graham A.W. & Caon, N., 2001, *MNRAS*, in press.
- van den Bergh, S., Abraham, R. G., Ellis, R. S., Tanvir, N. R., & Glazebrook, K. G. 1996, *AJ*, 112, 359
- White, S.D.M. 1983, in *Dynamics and Interactions of Galaxies*, ed. E. Athanassoula (Dordrecht; Reidel), 337
- Wirth, G.D., Koo, D. C. & Kron, R. G. 1994, *ApJ*, 435, L105

Young, C. K. & Currie, M. J. 1994, MNRAS, 268, L11

Fig. 1.— *Left from the top downwards:* a) Relative error in the total recovery magnitude versus the total input magnitude. b) Relative error of the output effective seeing-deconvolved radius versus the total input magnitude. c) Relative error of the output Sérsic index versus the total input magnitude. d) The difference  $\Delta\epsilon = \epsilon(\text{output}) - \epsilon(\text{input})$  between measured and input ellipticity versus the total input magnitude. *Right from the top downwards:* Mean relative errors of the quantities shown in the left column with  $1\sigma$  error bars.

Fig. 2.— Difference,  $\Delta n$ , between measured and input Sérsic indices versus input Sérsic index. Two different magnitude intervals ( $I < 19.5$  mag [solid circles],  $I > 19.5$  mag [open triangles]) are shown.

Fig. 3.— *Upper panel:* The recovery bulge parameters are shown. *Left from the top downwards:* a) Relative error of the total recovery magnitude versus the total input magnitude. b) Relative error of the output effective seeing-deconvolved radius versus the total input magnitude. c) Relative error of the output Sérsic index versus the total input magnitude. d) The difference  $\Delta\epsilon = \epsilon_b(\text{output}) - \epsilon_b(\text{input})$  between measured and input bulge ellipticity versus the total input magnitude. *Right from the top downwards:* Mean relative errors in the quantities shown in the left column with  $1\sigma$  error bars. *Lower panel:* The recovery disk parameters are shown. *Left from the top downwards:* a) Relative error of the total recovery magnitude versus the total input magnitude. b) Relative error of the output seeing-deconvolved scale length versus the total input magnitude. c) The difference  $d\epsilon = \epsilon_d(\text{output}) - \epsilon_d(\text{input})$  between measured and input disk ellipticity versus the total input magnitude. *Right from the top downwards:* Mean relative errors of the quantities shown in the left column with  $1\sigma$  error bars.

Fig. 4.— *Top left:* The difference,  $d(B/T)$ , between measured (output) and input bulge-to-total luminosity ratios versus seeing-deconvolved (i.e. model) scale length,  $h$ , for two different magnitude intervals ( $I < 18.5$  mag [solid circles],  $I > 18.5$  mag [open triangles]). *Top right:* Mean difference,  $\text{mean } d(B/T)$ , between measured and input bulge-to-total luminosity versus model scale length with  $1\sigma$  error bars. *Bottom left:* The difference,  $d(B/T)$ , between measured and input  $B/T$  versus the  $B/T(\text{input})$  for two different magnitude intervals ( $I < 18.5$  mag [solid circles],  $I > 18.5$  mag [open triangles]). *Bottom right:* Mean difference,  $\text{mean } d(B/T)$ , between measured and input  $B/T$  versus  $B/T(\text{input})$  with  $1\sigma$  error bars.

Fig. 5.— The  $I$ -band image of the central part of the cluster A2443 observed at the NOT.

Fig. 6.— Galaxies of the cluster A2443 for which structural parameters have been estimated. From left to right is represented a gray-scale image of the  $I$  band data (surface brightness isocontours are shown to  $\mu_I=23$  mag arcsec $^{-2}$  with steps of 1 mag arcsec $^{-2}$ ), the surface brightness profile, the ellipticity, and the residuals of the fit. Superimposed on the surface brightness profile data are the intrinsic profile (dashed line) and the convolution of this model profile (solid line) to match the data. The solid lines in the ellipticity plots show the fit to the ellipticities using our algorithm. Intrinsic ellipticities (i.e. not seeing convolved) of the galaxies can be obtained by extrapolating to



infinity the solid lines.

Fig. 7.— Color-magnitude diagram for the central region of A2443. Galaxies with  $I < 19$  mag (open symbols) were analyzed (see text).

Fig. 8.— *Top*:  $n$  versus bulge-to-disk ratio for galaxies with  $B/T < 0.6$  *Bottom*: Relation between disk size and luminosity for galaxies with  $B/T < 0.6$ .

Fig. 9.— *Top left*: The index  $n$  versus the distance to the brightest cluster member. The values of  $n$  shown correspond to the galaxies referred as “ellipticals”. *Top right*: The index  $n$  versus the distance to the brightest cluster member. The values of  $n$  presented correspond to the bulge component of the galaxies with  $B/T < 0.6$ . *Bottom left*: The index  $n$  versus the local surface density. The values of  $n$  shown correspond to the galaxies referred to as “ellipticals”. *Bottom right*: The index  $n$  versus the local surface density. The values of  $n$  presented here correspond to the bulge component of the galaxies with  $B/T < 0.6$ . Regression lines to all the points (solid lines) and excluding object 11 (dashed lines) are plotted.

Fig. 10.— *Top left*: The central galaxy concentration versus the distance to the brightest cluster member. The values of  $C$  shown correspond to the galaxies referred as “ellipticals”. *Top right*:  $C$  versus the distance to the brightest cluster member. The values of  $C$  presented correspond to the bulge component of the galaxies with  $B/T < 0.6$ . *Bottom left*:  $C$  versus the local surface density. The values of  $C$  shown correspond to the galaxies referred to as “ellipticals”. *Bottom right*:  $C$  versus the local surface density. The values of  $C$  presented here correspond to the bulge component of the galaxies with  $B/T < 0.6$ . All the values were established with  $\alpha = 0.3$ . Regression lines to all the points (solid lines) and excluding object 11 (dashed lines) are plotted.

Table 1. Mean relative errors for the bulge parameters

mag	16.25	16.75	17.25	17.75	18.25	18.75	19.25	19.75
$\text{mean}(\frac{\Delta mag}{mag})^a$	0.6±0.4	0.9±0.5	0.5±0.5	0.9 ± 0.6	1.0 ± 0.8	1.0±0.6	0.7±0.9	1.6±1.9
$\text{mean}(\frac{\Delta r_e}{r_e})^a$	−3.5±3.1	−1.5±4.2	−3.6±4.1	−0.9±4.0	0.1±6.6	2.3±6.1	0.9±1.0	11.2±17.6
$\text{mean}(\frac{\Delta n}{n})^a$	−1.4±1.4	−1.2±1.9	0.7±1.9	0.7±2.1	1.7±1.7	0.8±4.2	3.6±11.2	14.3±22.3
$\text{mean}(\epsilon_{\text{out}} - \epsilon_{\text{in}})$	−0.02±0.03	−0.01±0.02	−0.01±0.02	−0.02±0.02	−0.03±0.02	−0.03±0.06	0.04±0.09	0.05±0.13

<sup>a</sup>In %.

Table 2. Mean relative errors for the bulge and disk parameters

mag	16.25	16.75	17.25	17.75	18.25	18.75	19.25	19.75
$\text{mean}(\frac{\Delta mag}{mag})^{a,b}$	$-0.1 \pm 1.4$	$0.01 \pm 1.1$	$-1.0 \pm 1.2$	$-1.4 \pm 2.8$	$-2.1 \pm 2.7$	$-2.1 \pm 3.2$	$-1.4 \pm 2.7$	$-0.8 \pm 3.11$
$\text{mean}(\frac{\Delta r_e}{r_e})^a$	$0.1 \pm 8.7$	$-2.0 \pm 12.0$	$-2.2 \pm 13.0$	$-8.0 \pm 12.0$	$-21.8 \pm 42.06$	$-31.1 \pm 35.61$	$-16.5 \pm 46.9$	$-8.4 \pm 30.6$
$\text{mean}(\frac{\Delta n}{n})^a$	$9.6 \pm 6.8$	$1.7 \pm 7.8$	$4.8 \pm 6.7$	$-4.6 \pm 8.2$	$-6.3 \pm 13.5$	$-8.4 \pm 17.7$	$-26.7 \pm 38.29$	$-13.05 \pm 40.1$
$\text{mean}(\epsilon_{\text{out}} - \epsilon_{\text{in}})^b$	$-0.06 \pm 0.05$	$-0.03 \pm 0.07$	$-0.02 \pm 0.03$	$-0.04 \pm 0.07$	$-0.03 \pm 0.15$	$0.01 \pm 0.16$	$0.11 \pm 0.20$	$-0.03 \pm 0.10$
$\text{mean}(\frac{\Delta mag}{mag})^{a,c}$	$-0.1 \pm 0.2$	$0.01 \pm 0.01$	$-0.9 \pm 1.0$	$-0.8 \pm 0.8$	$-0.9 \pm 0.9$	$0.6 \pm 0.5$	$-0.9 \pm 1.0$	$3.5 \pm 3.1$
$\text{mean}(\frac{\Delta h}{h})^a$	$1.1 \pm 2.6$	$9.7 \pm 1.7$	$1.7 \pm 2.4$	$6.7 \pm 21.5$	$-3.7 \pm 12.5$	$-3.3 \pm 26.5$	$8.4 \pm 25.8$	$13.9 \pm 32.3$
$\text{mean}(\epsilon_{\text{out}} - \epsilon_{\text{in}})^c$	$0.01 \pm 0.02$	$0.01 \pm 0.04$	$0.02 \pm 0.05$	$0.02 \pm 0.03$	$0.03 \pm 0.11$	$0.08 \pm 0.18$	$0.14 \pm 0.14$	$-0.07 \pm 0.24$

<sup>a</sup>In %.

<sup>b</sup>Bulge parameter.

<sup>c</sup>Disk parameter.

Table 3. Broad-band photometry (Johnson filters) of the core of Abell 2443

ID	R.A. (2000)	Dec. (2000)	<i>B</i>	<i>V</i>	<i>R</i>	<i>I</i>
1	22:26:07.92	17:21:24.9	16.44	15.17	14.83	13.97
2	22:26:04.61	17:21:55.4	19.02	17.69	17.35	16.52
3	22:26:01.86	17:22:35.3	23.23	23.42	19.59	17.42
4	22:26:02.38	17:22:17.8	19.37	17.85	17.27	16.55
5	22:26:01.65	17:22:53.0	20.72	19.87	19.23	18.16
6	22:26:02.72	17:22:26.3	20.22	18.77	18.28	17.52
7	22:26:02.21	17:22:46.9	17.68	16.27	15.86	15.05
8	22:26:01.76	17:19:42.8	19.67	19.62	19.58	17.82
9	22:26:02.76	17:20:04.4	20.22	19.32	18.87	18.21
10	22:26:02.42	17:21:50.8	19.63	18.21	17.80	16.95
11	22:26:02.26	17:21:41.2	20.42	19.01	18.59	17.77
12	22:26:01.59	17:21:45.5	23.37	21.72	20.41	19.29
13	22:26:01.61	17:20:52.2	25.79	23.05	22.18	20.36
14	22:26:01.57	17:20:23.0	24.28	23.33	22.79	22.21
16	22:26:14.36	17:22:37.2	23.39	22.60	22.27	21.70
17	22:26:13.98	17:20:52.9	23.35	23.20	22.55	21.75
18	22:26:13.88	17:21:47.5	22.62	21.80	21.19	20.42
19	22:26:13.90	17:21:26.6	24.01	23.12	22.42	21.45
20	22:26:13.77	17:20:15.8	23.00	21.90	20.79	19.60
21	22:26:13.71	17:20:43.5	22.53	21.28	20.78	19.97
22	22:26:13.70	17:20:24.5	23.92	22.63	22.20	21.63
23	22:26:13.60	17:20:51.6	22.22	20.97	20.51	19.78
25	22:26:13.28	17:22:43.1	23.95	22.99	22.37	21.40
26	22:26:13.18	17:19:38.8	22.21	20.55	19.53	18.41
27	22:26:12.98	17:21:09.7	20.86	19.37	18.94	18.11
28	22:26:12.56	17:22:35.4	21.86	20.47	19.89	19.40
29	22:26:12.74	17:20:12.8	22.58	21.14	20.13	18.98
30	22:26:12.72	17:20:32.5	24.73	23.23	22.73	22.04
31	22:26:12.57	17:20:11.1	23.32	22.38	21.77	20.99
32	22:26:12.48	17:21:44.6	21.32	20.25	19.95	19.34
33	22:26:12.56	17:21:19.5	24.44	23.10	22.70	21.98
34	22:26:12.51	17:22:51.6	24.41	22.94	20.73	22.06
35	22:26:11.93	17:20:47.1	19.80	18.35	17.94	17.07
36	22:26:11.44	17:21:40.8	23.59	22.25	21.95	21.46
37	22:26:11.47	17:19:46.4	24.14	22.65	21.77	20.79
38	22:26:11.08	17:21:52.9	21.24	19.91	19.51	18.71
39	22:26:10.96	17:20:31.9	19.84	18.39	17.95	17.11
40	22:26:10.88	17:22:06.2	21.26	19.98	19.42	18.60
41	22:26:10.92	17:21:06.2	23.57	22.05	21.66	20.93
42	22:26:10.80	17:22:38.4	22.06	20.94	20.67	19.97
43	22:26:10.80	17:21:04.6	24.02	22.22	21.96	20.87
44	22:26:10.53	17:21:24.8	20.44	19.00	18.59	17.82
45	22:26:10.46	17:22:04.6	21.79	20.41	20.02	19.25
46	22:26:10.49	17:20:58.8	23.55	22.67	22.39	21.86
47	22:26:10.37	17:21:37.8	22.11	20.91	20.51	19.79
48	22:26:10.39	17:20:23.6	21.24	19.85	19.50	18.67
49	22:26:10.11	17:20:49.5	20.89	19.86	19.45	18.65
50	22:26:10.23	17:22:50.4	21.43	20.71	20.39	19.69
51	22:26:10.34	17:22:10.8	24.23	22.82	22.56	21.94

Table 3—Continued

ID	R.A. (2000)	Dec. (2000)	<i>B</i>	<i>V</i>	<i>R</i>	<i>I</i>
52	22:26:10.10	17:21:04.5	22.42	21.10	20.76	19.93
53	22:26:09.91	17:21:14.8	22.16	20.91	22.19	19.89
54	22:26:09.92	17:21:29.3	22.55	21.10	20.46	19.17
55	22:26:10.38	17:20:47.7	22.96	20.69	20.39	19.62
56	22:26:09.37	17:21:09.8	23.19	22.60	22.13	21.93
57	22:26:09.38	17:20:32.6	23.20	22.44	22.35	22.05
58	22:26:09.38	17:19:46.5	23.48	22.65	21.98	21.15
59	22:26:09.29	17:22:09.2	24.49	22.91	22.30	21.65
61	22:26:07.35	17:21:40.5	19.76	18.22	17.78	17.12
62	22:26:08.09	17:21:52.6	20.69	19.45	19.09	18.31
63	22:26:08.00	17:21:47.9	19.40	18.11	17.70	16.91
64	22:26:08.71	17:19:38.1	23.89	21.96	21.18	20.09
65	22:26:08.25	17:20:50.8	20.60	19.14	19.00	17.87
66	22:26:09.05	17:21:51.6	23.49	22.25	22.29	21.94
68	22:26:08.18	17:19:41.9	21.93	20.56	20.26	19.41
69	22:26:08.18	17:19:55.0	23.83	23.47	23.02	22.35
70	22:26:08.41	17:19:48.5	23.86	22.97	24.71	20.69
71	22:26:07.88	17:19:54.8	22.92	21.49	21.08	20.58
72	22:26:07.83	17:22:32.9	23.16	21.59	20.95	19.39
73	22:26:07.69	17:22:08.9	23.17	22.69	21.95	21.22
74	22:26:07.48	17:22:53.3	20.42	19.36	18.98	18.19
75	22:26:07.46	17:19:34.9	20.64	19.66	19.32	18.53
76	22:26:07.43	17:20:44.1	23.47	22.80	22.15	21.31
77	22:26:07.32	17:21:24.3	19.91	18.32	17.93	17.14
78	22:26:07.01	17:21:52.5	24.28	23.02	22.78	22.22
79	22:26:07.09	17:19:40.8	23.95	23.85	23.26	22.00
80	22:26:06.94	17:19:38.6	23.91	21.34	20.48	19.23
81	22:26:06.76	17:19:39.6	21.85	20.57	20.20	19.40
82	22:26:06.47	17:22:07.9	20.24	18.76	18.37	17.54
83	22:26:06.51	17:19:53.9	23.14	21.57	20.73	19.67
84	22:26:06.40	17:21:52.0	24.02	22.91	22.40	21.82
85	22:26:08.81	17:20:45.4	22.29	20.75	20.06	18.83
86	22:26:06.56	17:22:02.3	23.57	21.62	20.93	18.98
87	22:26:06.13	17:21:58.1	22.35	21.70	21.63	20.99
88	22:26:06.17	17:22:00.0	24.95	23.52	23.12	21.71
89	22:26:06.22	17:19:45.8	22.75	21.52	21.14	20.32
90	22:26:05.81	17:22:17.1	20.73	19.81	19.52	18.91
91	22:26:05.88	17:21:52.2	24.12	22.57	23.04	21.51
92	22:26:05.82	17:21:28.0	23.67	22.84	22.65	21.53
93	22:26:05.85	17:20:31.3	23.02	22.41	21.95	20.89
94	22:26:05.75	17:22:27.4	22.57	21.17	20.81	20.01
95	22:26:05.69	17:21:16.5	23.53	22.46	21.99	21.21
96	22:26:05.73	17:21:44.6	24.31	23.31	22.80	21.55
97	22:26:05.75	17:20:01.2	22.12	21.09	20.79	19.98
98	22:26:05.73	17:19:37.7	22.99	21.81	21.41	20.82
99	22:26:05.23	17:20:55.7	23.11	21.44	20.92	20.00
100	22:26:05.18	17:21:50.5	23.40	21.87	21.23	20.50
101	22:26:05.21	17:21:27.5	24.05	23.72	27.27	22.25
102	22:26:04.94	17:22:51.6	22.70	22.51	21.87	21.22

Table 3—Continued

ID	R.A. (2000)	Dec. (2000)	<i>B</i>	<i>V</i>	<i>R</i>	<i>I</i>
103	22:26:04.79	17:20:32.2	24.82	23.29	22.68	22.40
104	22:26:04.37	17:21:36.2	19.92	18.52	18.14	17.31
105	22:26:04.36	17:22:31.8	23.27	23.01	22.69	22.13
106	22:26:04.41	17:20:40.1	23.88	23.04	22.50	22.13
107	22:26:04.10	17:22:37.8	22.77	21.80	21.46	20.62
108	22:26:03.63	17:20:53.8	23.26	22.37	22.03	21.60
109	22:26:05.00	17:21:03.1	24.51	23.13	22.34	22.07
113	22:26:02.70	17:22:14.3	23.18	21.25	20.81	20.06
114	22:26:15.27	17:19:59.6	22.50	22.51	22.08	20.89
116	22:26:03.20	17:21:20.8	24.52	23.09	22.43	20.78
117	22:26:15.17	17:20:31.1	22.14	22.51	21.65	20.31
118	22:26:02.91	17:22:17.4	23.96	22.48	22.19	21.75
119	22:26:02.84	17:21:41.7	24.25	23.47	22.69	21.59
120	22:26:02.75	17:20:57.1	21.40	20.12	19.65	18.98
121	22:26:02.62	17:21:40.2	24.28	22.88	22.51	22.40
122	22:26:02.64	17:20:38.5	23.32	22.70	22.04	21.82
123	22:26:02.53	17:21:30.4	22.99	22.15	21.38	20.57
124	22:26:02.07	17:20:14.8	23.66	22.35	22.63	20.97
125	22:26:01.86	17:22:08.9	24.04	22.62	22.54	21.38
126	22:26:01.76	17:21:04.2	23.68	22.97	22.58	21.58
127	22:26:14.74	17:21:02.3	21.63	20.84	20.38	19.71
128	22:26:14.75	17:20:58.9	23.75	22.77	22.06	21.10
129	22:26:14.41	17:22:15.3	22.07	20.53	19.42	18.39

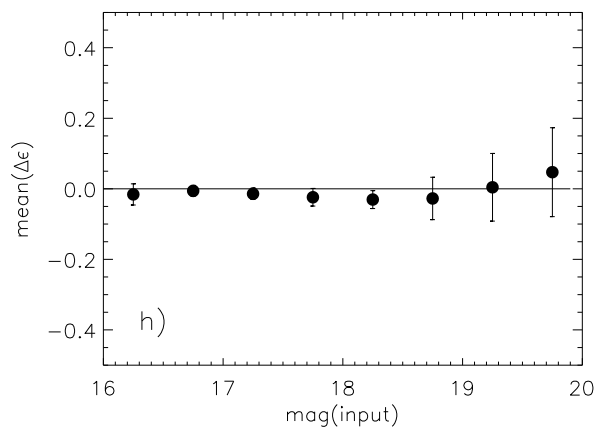
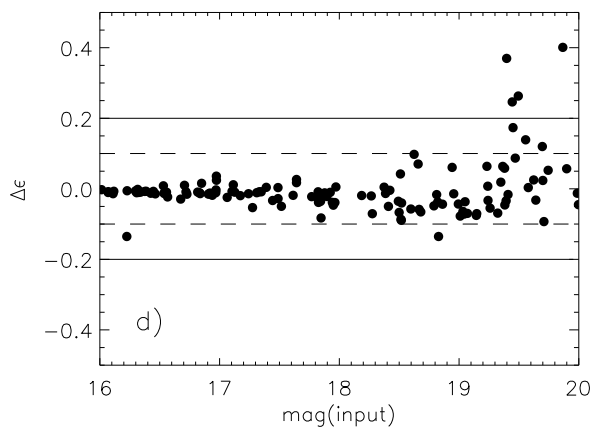
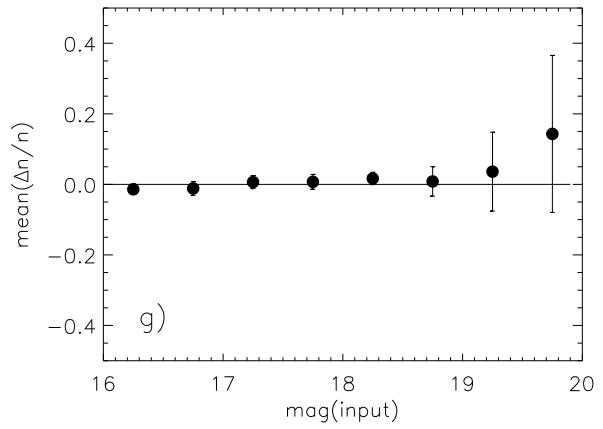
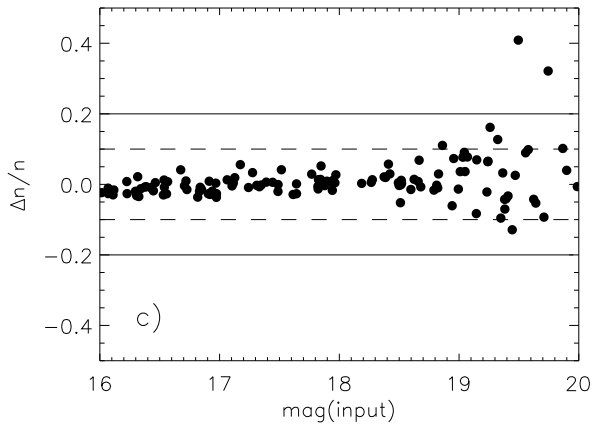
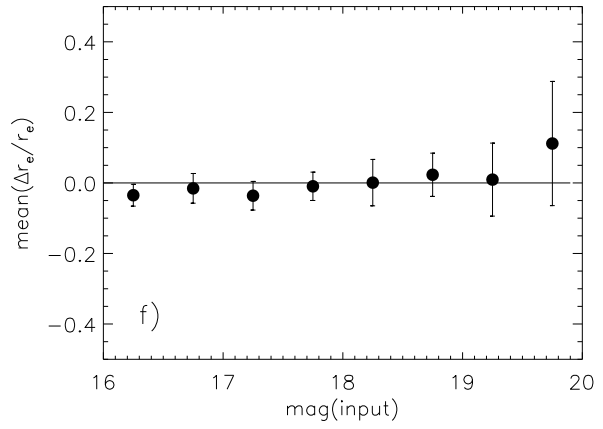
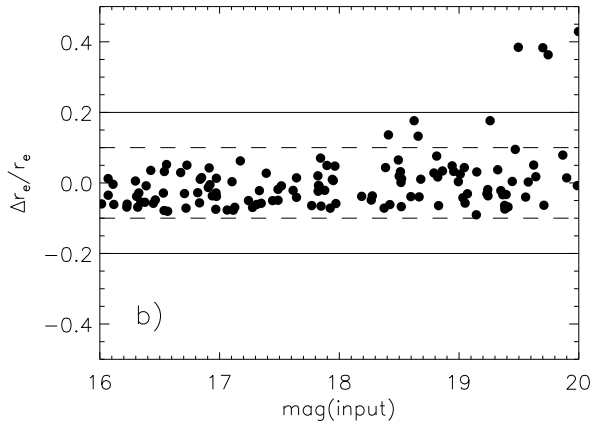
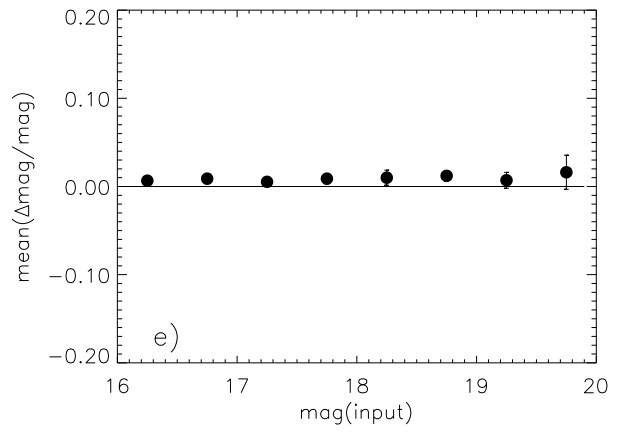
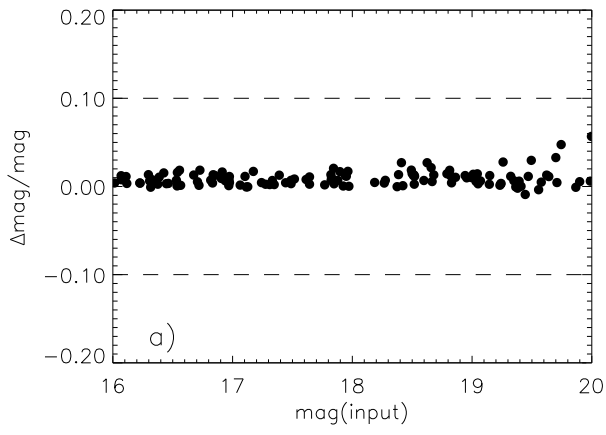
Table 4. Parameters of the bulge and disk decomposition for objects with  $B/T < 0.6$

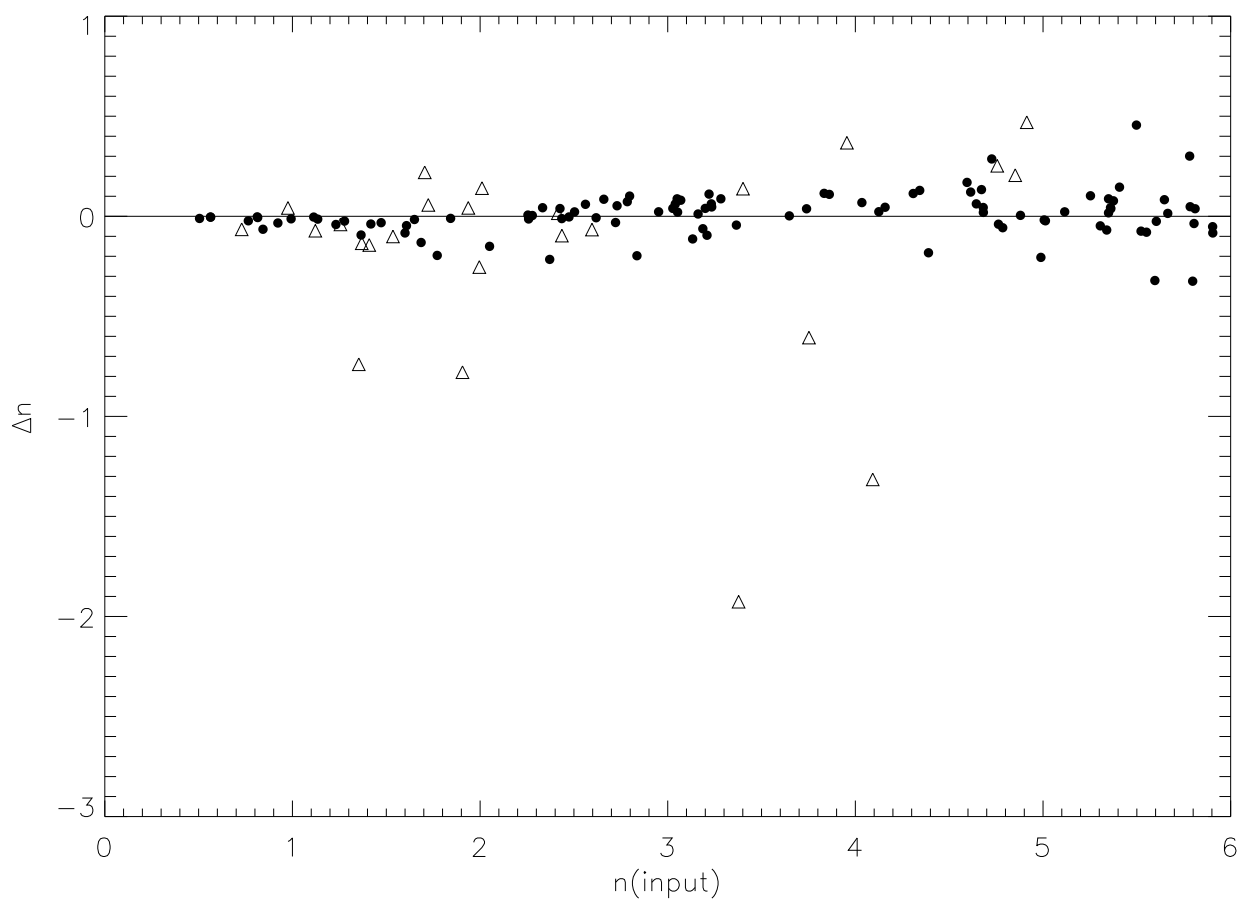
ID	$I_e$ (mag arcsec $^{-2}$ )	$r_e$ (arcsec)	$n$	$\epsilon_b$	$I_0$ (mag arcsec $^{-2}$ )	$h$ (arcsec)	$\epsilon_d$	$B/T$
1	$19.46 \pm 0.05$	$1.73 \pm 0.15$	$1.17 \pm 0.05$	0.05	$19.53 \pm 0.19$	$4.94 \pm 0.64$	0.12	0.23
7	$19.92 \pm 0.08$	$1.43 \pm 0.08$	$2.61 \pm 0.08$	0.12	$20.71 \pm 0.12$	$5.44 \pm 0.64$	0.19	0.31
39	$18.71 \pm 0.40$	$0.40 \pm 0.11$	$2.25 \pm 0.66$	0.25	$20.06 \pm 0.39$	$1.31 \pm 0.23$	0.01	0.39
63	$17.88 \pm 0.24$	$0.22 \pm 0.02$	$0.62 \pm 0.75$	0.20	$19.73 \pm 0.11$	$1.45 \pm 0.12$	0.11	0.15
65	$20.01 \pm 0.3$	$0.48 \pm 0.10$	$3.24 \pm 0.82$	0.16	$20.31 \pm 0.33$	$1.15 \pm 0.23$	0.19	0.44
82	$18.16 \pm 0.25$	$0.31 \pm 0.03$	$0.76 \pm 0.55$	0.56	$18.91 \pm 0.21$	$0.90 \pm 0.09$	0.37	0.23

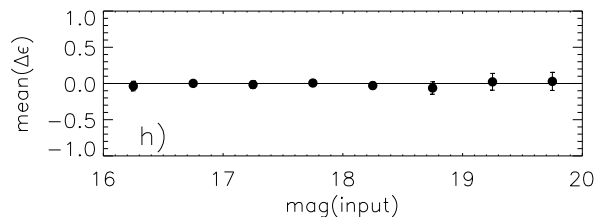
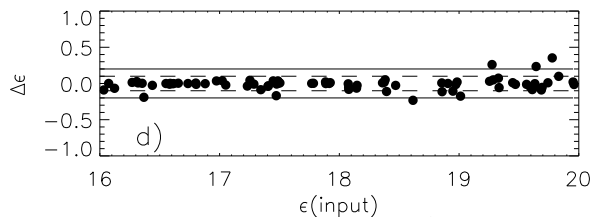
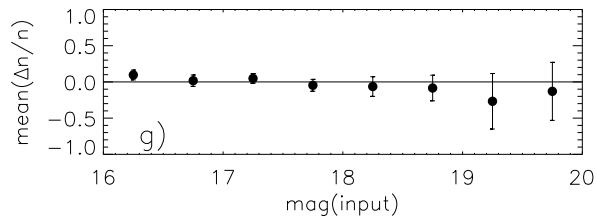
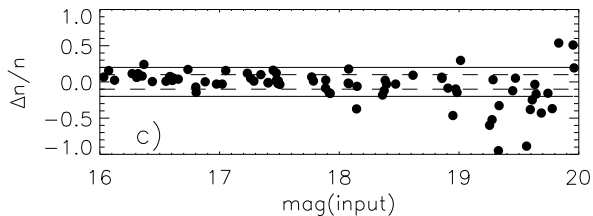
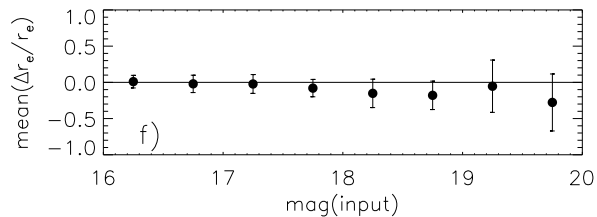
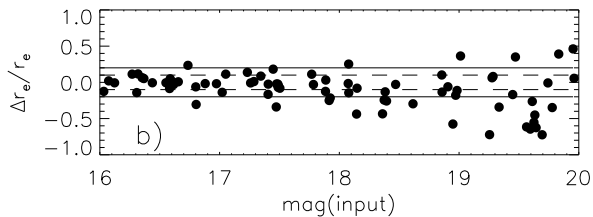
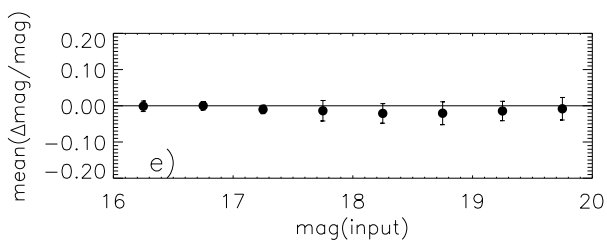
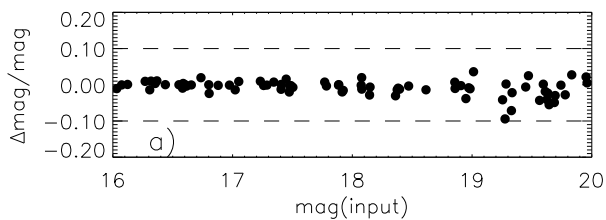
Table 5. Parameters of objects with  $B/T > 0.6$  (elliptical objects)

ID	$I_e$ (mag arcsec $^{-2}$ )	$r_e$ (arcsec)	$n$	$\epsilon_b$
4	$21.60 \pm 0.04$	$2.86 \pm 0.07$	$3.91 \pm 0.06$	0.12
6	$27.36 \pm 0.24$	$66.37 \pm 10.16$	$10.05 \pm 0.33$	0.53
9	$23.14 \pm 0.75$	$3.20 \pm 1.99$	$3.46 \pm 1.16$	0.38
10	$21.12 \pm 0.05$	$1.72 \pm 0.05$	$3.60 \pm 0.07$	0.03
11	$22.09 \pm 0.06$	$2.26 \pm 0.08$	$7.38 \pm 0.19$	0.43
26	$23.23 \pm 0.10$	$2.53 \pm 0.14$	$8.82 \pm 0.36$	0.17
27	$20.91 \pm 0.01$	$0.97 \pm 0.01$	$3.76 \pm 0.02$	0.21
29	$22.68 \pm 0.47$	$1.53 \pm 0.46$	$5.83 \pm 1.08$	0.24
38	$21.81 \pm 0.49$	$1.29 \pm 0.41$	$2.87 \pm 0.81$	0.27
44	$21.35 \pm 0.18$	$1.62 \pm 0.16$	$4.49 \pm 0.30$	0.33
48	$20.98 \pm 0.22$	$1.02 \pm 0.12$	$1.74 \pm 0.29$	0.31
61	$21.72 \pm 0.57$	$1.86 \pm 0.71$	$6.81 \pm 1.29$	0.14
74	$21.39 \pm 0.11$	$1.74 \pm 0.12$	$0.81 \pm 0.08$	0.24
75	$21.73 \pm 0.17$	$1.79 \pm 0.18$	$1.31 \pm 0.17$	0.52
85	$15.57 \pm 0.60$	$0.04 \pm 0.02$	$8.87 \pm 7.84$	0.10
86	$15.02 \pm 0.08$	$0.03 \pm 0.01$	$12.29 \pm 2.97$	0.01
104	$20.84 \pm 0.16$	$1.66 \pm 0.15$	$3.21 \pm 0.22$	0.32
120	$22.27 \pm 0.20$	$1.41 \pm 0.16$	$3.41 \pm 0.34$	0.25
129	$22.29 \pm 0.04$	$1.58 \pm 0.04$	$4.79 \pm 0.16$	0.10









Disk parameters

